7

Shock-Induced Turbulent Boundary Layer Separation in Over-Expanded Rocket Nozzles: Physics, Models, Random Side Loads, and the Diffusive Character of Stochastic Rocket Ascent

R. G. Keanini, T. D. Nortey, Karen Thorsett-Hill, N. Srivastava,
Sam Hellman, P. T. Tkacik and P. Douglas Knight
Department of Mechanical Engineering & Engineering Science
The University of North Carolina at Charlotte
USA

1. Introduction

Contrary to popular belief, and notwithstanding two hundred years of scientific study (Gruntman , 2004), the problem of accurately predicting rocket ascent remains largely unsolved. The difficulties trace to a variety of altitude-, speed-, and launch-site-dependent random forces that act during rocket ascent, including: i) aerodynamic forces (Sutton & Biblarz, 2001), ii) forces due to wind and atmospheric turbulence (Flemming et al., 1988; Justus & Johnson, 1999; Justus et al., 1990; Leahy, 2006), iii) forces produced by rocket construction imperfections (Schmucker, 1984), and iv) impacts with air-borne animals and debris (McNaughtan, 1964). Significantly, our physical understanding and ability to model the dynamical effects of each of these random features is fairly well-developed.

By contrast, understanding of the *physical origins,* as well as the *dynamical effects* of altitude-dependent, in-nozzle *random side loads,* has only recently begun to emerge (Keanini et al., 2011; Ostlund, 2002; Srivastava et al., 2010). Referring to figures 1 through 3, we find that side loads represent the end result of a chain of in-nozzle fluid dynamic processes. During low altitude flight, under over-expanded flight conditions, a pressure gradient can exist between the high pressure ambient air surrounding the rocket and nozzle, and the low pressures extant within the nozzle. This pressure gradient can force ambient air *upstream* along the nozzle wall; eventually, inertia of the ambient inflow is overcome by the pressure and inertial forces associated with the outflow, producing a near-wall recirculation region. To the supersonic flow outside the near-wall boundary layer, the recirculation zone functions as a virtual compression corner, producing an oblique shock (Keanini & Brown, 2007; Ostlund, 2002; Summerfield et al., 1954). See figures 1 through 3. Due to the altitude dependence of $P_a = P_a(H(t))$, where P_a is the ambient pressure and $H(t)$ is the rocket's time-dependent altitude, the nominal location of the oblique shock, $x_{shock} = x_{shock}(H(t))$, also varies with altitude.

Random side loads arise due to two coupled flow features: i) The oblique shock produces a sharp, adverse pressure rise within the near-wall outflow boundary layer, forcing the boundary layer to separate from the nozzle wall; see figure 1. ii) The *shape* of the boundary

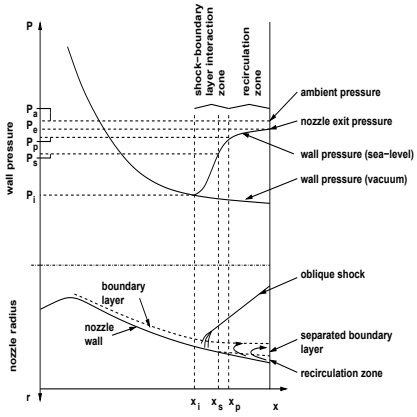

Fig. 1. Schematic of shock-induced boundary layer separation in rocket nozzles. The pressure variation shown is characteristic of free interaction separation problems. Adapted from Ostlund (2002).

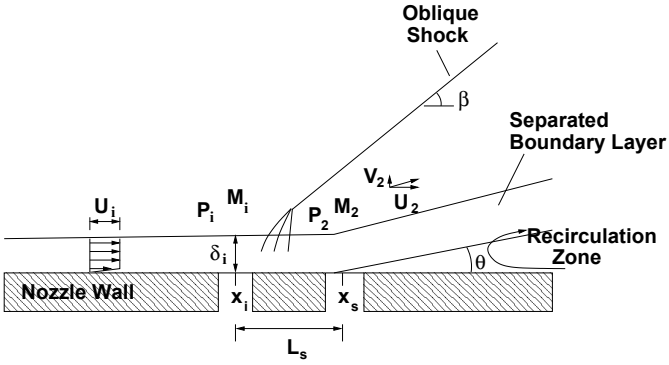

Fig. 2. Shock-induced boundary layer separation in overexpanded supersonic nozzle flow. The process typically occurs during low altitude flight when ambient pressure is high enough to force atmospheric air into the nozzle. The incoming air flows upstream along the low-inertia, near-wall region until downstream-directed boundary layer inertia turns it, forming a virtual compression corner. An oblique shock thus forms, and the combined action of shock-induced pressure rise and inertial pressurization produced by the inflow forces the down-flow boundary layer to separate. Pressures, mach numbers, and velocities are denoted, respectively, by P, M, and U and V. Axial positions where the boundary layer starts to thicken (i denotes *incipient*), and where it separates are denoted, respectively, as x_i and x_s; the nominal shock-boundary layer interaction zone is shown as L_s. Since the separation line position, x_s, and downstream conditions vary with the altitude-dependent ambient pressure, $P_a = P_a(H(t))$ (Keanini & Brown, 2007), all variables shown likewise vary with $H(t)$.

layer separation line, which at any instant, forms a closed curve along the nozzle periphery, varies randomly in space and time; see figure 3. Due to relatively uniform pressure distributions extant on the up- and downstream sides of the instantaneous separation line

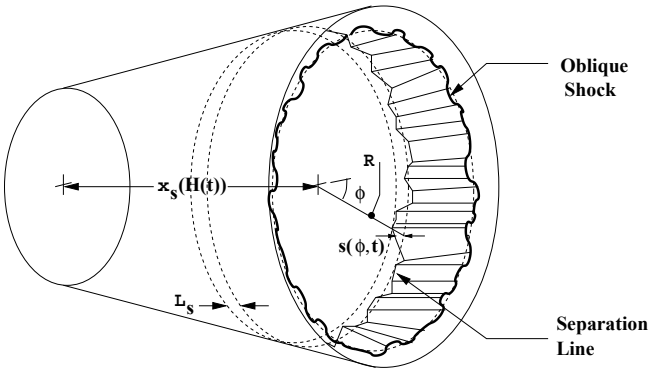

Fig. 3. Schematic of stochastic boundary layer separation line and associated, rippled, azimuthal oblique shock. The mean separation line position relative to the nozzle throat, x_s, varies with rocket altitude, $H(t)$; the corresponding nozzle radius is $R = R(H(t))$. The instantaneous separation line position relative to $x_s(t)$ is shown as $s(\phi, t)$. The separation line lies on the nozzle wall and, in a nominally symmetric nozzle, the shock forms an azimuthally independent, average angle which varies with $x_s(t)$. Adapted from (Keanini et al., 2011).

(Keanini et al., 2011; Srivastava et al., 2010) - where fore and aft pressures, determined by the shock, differ significantly - a net, time- dependent side force, or *side load*, $\mathbf{F_s}$, is produced.

1.1 Connection to mass transfer

From a mass transfer perspective, a deep and unanticipated connection exists between the stochastic ascent of rockets subjected to side loading and damped diffusion processes. In order to understand the complex physical origins of this connection, it is necessary to first consider the purely mechanical features that connect shock-induced boundary layer separation to stochastic rocket response. Thus, much of this Chapter describes recent work focused on understanding these connections (Keanini et al., 2011; Srivastava et al., 2010). From a technological standpoint, the importance of separation-induced side loads derives from their sometimes catastrophic effect on rocket ascent. Side loads have been implicated, for example, in the in-flight break-up of rockets (Sekita et al., 2001), and in the failure of various rocket engine components (Keanini & Brown, 2007).

1.2 Chapter objectives

The objectives of this Chapter are as follows:

I) Two stochastic models (Keanini et al., 2011; Srivastava et al., 2010) and two simple (deterministic) scaling models (Keanini & Brown, 2007) have recently been proposed to describe shock-induced boundary layer separation within over-expanded rocket nozzles (Keanini & Brown, 2007; Keanini et al., 2011; Srivastava et al., 2010). Earlier work, carried out in the 1950's and 60's and focused on time-averaged separation behavior, lead to development of the Free Interaction model of boundary layer separation (Carriere et al., 1968; Chapman et al., 1958; Erdos & Pallone, 1962; Keanini & Brown, 2007; Ostlund, 2002). Our first objective centers on describing the physical bases underlying these models, as well as highlighting experimental evidence that supports the validity of each.

II) The stochastic boundary layer separation models developed in (Keanini et al., 2011; Srivastava et al., 2010) allow construction of stochastic side load models that, on one hand, are physically self-consistent, and on the other, are imbued with statistical properties that are fully consistent with available experimental observations. Our second objective focuses on describing these new stochastic side load models.

III) Given physically consistent separation and side load models (Keanini et al., 2011; Srivastava et al., 2010), the effect of random nozzle side loads on rocket ascent can be computed. Our group recently developed (Keanini et al., 2011) a series of interconnected, analytical models describing: i) fast time-scale, altitude-dependent stochastic boundary layer separation, ii) associated short-time- and long(rocket-dynamics)-time-scale stochastic side load generation, and iii) stochastic, altitude-dependent rocket response. In addition, a high-fidelity numerical model which solved the full nonlinear, coupled equations of rocket rotational and translational motion, under the action of altitude-dependent random side loads, was also reported (Srivastava et al., 2010). Our third objective centers on outlining these analytical and numerical models, and on describing recent results.

IV) Our most recent work (Keanini et al., 2011) demonstrates that rocket pitch and yaw rates evolve as Ornstein-Uhlenbeck processes. Since stochastic pitch and yaw rate evolution determines not only the random evolution of pitch/yaw displacement, but also the stochastic evolution of the rocket's lateral velocity and displacement (Keanini et al., 2011), the rocket's rotational and translational dynamics, fundamentally, trace to a damped diffusion process. The last objective centers on highlighting the connection between stochastic side load-driven rocket response and Ornstein-Uhlenbeck diffusion.

2. Boundary layer separation models and mean separation location

Two physically-based models of shock-induced separation were developed in 2007 (Keanini & Brown, 2007). The models assume importance for two reasons. First, they provide verifiable insight into the physical processes underlying shock-separation of compressible turbulent boundary layers. Second, they allow prediction of the altitude-dependent mean separation line, crucial in determining both the location and magnitude of altitude-dependent random side loads (Keanini et al., 2011; Srivastava et al., 2010). This section describes the more refined of these two models, as well as Chapman's Free Interaction Model (Chapman et al., 1958). All three models rely on scaling analyses of the boundary layer and near-boundary flows, in and near the boundary layer separation zone.

2.1 Time-average separation

Two distinct separation processes have been identified in overexpanded rocket nozzles, *free shock separation*, in which the turbulent boundary layer separates without reattachment, and *restricted shock separation*, in which the separated boundary layer reattaches, forming a small, closed recirculation zone immediately downstream of the separation point; see, e.g., (Keanini & Brown, 2007; Ostlund, 2002) for recent reviews of this work. This Chapter focuses on free shock separation.

The time-average flow features associated with free shock separation in nozzles were first characterized by Summerfield et al. (Summerfield et al., 1954), and are depicted schematically in figures 1 and 2. As shown, the time average pressure along the nozzle wall increases from P_i at the incipient separation point, x_i, to a peak value of P_p at x_p. Depending on the nozzle and the shock location relative to the nozzle exit, P_p is typically on the order of 80 to 100 % of

the ambient pressure, P_a. The time-average separation point, x_s, lies immediately upstream of x_p.

Of central importance in nozzle design is determining both the conditions under which separation will occur and the approximate separation location. A number of criteria have been proposed for predicting the nominal free shock separation point, x_s; see, e.g., (Keanini & Brown, 2007; Ostlund, 2002) for reviews. Since the boundary layer pressure rise between x_i and x_s depends primarily on the inviscid flow Mach number, M_i, most criteria relate either a gross separation pressure ratio, P_i/P_a, or more recently, a refined ratio, P_i/P_p, to M_i (Ostlund, 2002). Given the separation pressure ratio, the separation location can then be determined using an appropriate model of flow upstream of separation.

Although the actual separation process is highly dynamic, the scaling model focuses on time average flow dynamics in the vicinity of the shock interaction zone. In order to provide physical context, we briefly review the dynamical features associated with free shock separation and note simplifying assumptions made. Shock motion over the shock interaction zone appears to be comprised of essentially two components: i) a low frequency, large scale motion produced by flow variations downstream of the separation point, and occurring over the length of the shock interaction zone, $l_p = x_p - x_i$, at characteristic frequencies, f_s [on the order of 300 to 2000 Hz in the case of compression ramp and backward facing step flows (Dolling & Brusniak, 1989)], and ii) a high frequency, low amplitude jitter produced by advection of vortical structures through the shock interaction zone (Dolling & Brusniak, 1989). The scaling models in (Keanini & Brown, 2007) limit attention to time scales that are long relative to f_s^{-1}. In addition, the model assumes that the flow is statistically stationary and that the separation process is two-dimensional.

The time average pressure gradient over the shock interaction zone $(x_i \leq x \leq x_p)$, given approximately by

$$\frac{\partial P}{\partial x} \sim \frac{P_p - P_i}{l_p} \tag{1}$$

in reality reflects the intermittent, random motion of the shock between x_i and x_p; see, e.g., (Dolling & Brusniak, 1989). As the shock-compression wave system oscillates randomly above (and partially within) the boundary layer, the associated pressure jump across the system is transmitted across the boundary layer on a time scale $\tau_s \sim \delta_i/\sqrt{kRT_i}$, where δ_i and T_i are the characteristic boundary layer thickness and temperature in the vicinity of x_i. Under typical experimental conditions, τ_s is much shorter than the slow time scale, f_s^{-1} (where $\tau_s \approx$ 1 to $10\mu s$); thus, the instantaneous separation point essentially tracks the random position of the shock-compression wave system, where the position of the separation point is described by a Gaussian distribution over the length of the interaction zone (Dolling & Brusniak, 1989).

2.2 Scale analysis of shock-induced separation

In the vicinity of the separation point,x_s, we recognize that a fluid particle's normal acceleration component within the separating boundary layer is determined by the normal component of the pressure gradient across the separating boundary layer. Thus, balancing these terms (in the Navier- Stokes equations) yields:

$$\rho \frac{V_s^2}{R} \sim \frac{\partial P}{\partial n} \tag{2}$$

where V_s is the particle speed in the streamwise (s-)direction, and R^{-1} is the local streamline curvature. The curvature can be evaluated by first defining the shape of the boundary layer's

outer-most streamline (i.e., a streamline in the vicinity of δ which is roughly parallel to the local displacement thickness) as $r(x) = f(x)$, where $r(x)$ is the radial distance from the nozzle centerline to the streamline, evaluated at axial position x. Thus, $R^{-1} = f''(\sqrt{1+(f')^2})^{-3}$. Expressing V_s^2 in terms of local cartesian velocity components, $V_s^2 = u_s^2 + v_s^2$, and estimating u_s and v_s by their approximate free stream magnitudes downstream of the oblique shock (since again, at axial position x_s, the boundary layer has passed through the compression system below the shock), we obtain $V_s^2 \approx U_2^2 + V_2^2$. Replacing terms in (2) by their approximate magnitudes then leads to

$$\rho_2 \frac{U_2^2 + V_2^2}{R} \sim \frac{P_p - P_2}{\delta_s} \tag{3}$$

where arguments given in (Keanini & Brown, 2007) lead to the necessary pressure gradient and density estimates.

2.3 Boundary layer thickness

In order to proceed, we must estimate the magnitude of the boundary layer thickness, δ_s, immediately upstream of the separation point, x_s. First, note that at the wall between x_i and x_s, the x-momentum equation yields the approximate balance

$$\mu \frac{\partial^2 u}{\partial y^2} \sim \frac{\partial P}{\partial x} \tag{4}$$

where μ is the dynamic viscosity. Estimating the magnitude of each term in this equation leads to

$$\frac{U_2}{\delta_s^2} \sim \frac{1}{\mu} \frac{(P_p - P_1)}{l_s} \tag{5}$$

where, since we are focusing on the neighborhood of x_s, u is approximated as U_2, and where it is recognized that the streamwise pressure increases from approximately P_1 near x_i to approximately P_p near x_s. [Although P equals P_s at x_s, due to the relatively small difference between P_s and P_p, for simplicity, we approximate $P(x_s)$ as P_p.] The x-length scale, $l_s = (x_s - x_i)$, is approximately equal to the length of the shock interaction zone, $l_p = x_p - x_i$. Considering the continuity equation near x_s, we recognize that since the boundary layer acquires a vertical velocity component as it travels toward and past x_s, and since associated mass advection and volumetric dilatation terms, $\rho^{-1}\mathbf{u} \cdot \nabla\rho$, and $\nabla \cdot \mathbf{u}$, respectively, are of the same order, then

$$\frac{\partial u}{\partial x} \approx \frac{\partial v}{\partial y} \tag{6}$$

or in terms of orders of magnitude,

$$\frac{U_2}{l_s} \sim \frac{V_2}{\delta_s} \tag{7}$$

where again the vertical velocity near x_s is on the order of V_2, the inviscid flow's vertical velocity component immediately downstream of the oblique shock. Thus, since $V_2/U_2 \sim \tan\,\theta$, we obtain the following estimate for δ_s/l_s :

$$\delta_s/l_s \sim \tan\,\theta \tag{8}$$

Note that this relationship is analogous to one of the key assumptions underlying Chapman's (Chapman et al., 1958) free interaction model, viz, the displacement of the external inviscid

flow is determined by the streamwise rate of boundary layer growth. Using (8) in (5) and solving for δ_s finally yields an estimate for the boundary layer thickness near x_s :

$$\delta_s \sim \frac{\mu M_2 a_2 \cos\ \theta}{(P_p - P_1) tan\theta} \tag{9}$$

where $U_2 = M_2 a_2 \cos\theta$ and a_2 is the sound speed.
Before proceeding, and as an aside, we rewrite the estimate in (9) as

$$\frac{\mu U_2/\delta_s}{P_p - P_1} \sim \frac{\tau_2}{\Delta P} \sim \tan\ \theta \tag{10}$$

Recognizing that the resultant stress on a fluid particle near x_s is approximately equal to the vector sum of the horizontally acting viscous shear stress, τ_2, and the vertically-acting net pressure, $\Delta P = P_p - P_1$, then (10) shows that the resultant acts in the direction of the separating boundary layer, θ, as it must. Since $\delta_s/l_s \sim \tan\theta$, then (10) is also consistent with Chapman's (Chapman et al., 1958) estimate for $\tau_2/\Delta P$. Likewise, Chapman et al. (Chapman et al., 1958) argued that $\delta^*/l_s \sim C_f = \tau_w/(\rho_1 u_1^2/2)$, where C_f is the friction factor; since $\tau_w \sim \Delta P$, then for nominally fixed θ (see Sec. II.D below), (10) is also consistent with Chapman's estimate for C_f.
Returning to Eqn. (3), inserting (9) and the expression for R^{-1} and rearranging leads to an expression of the following form:

$$(\frac{P_p}{P_1})^2 - (1+G)\frac{P_p}{P_1} + G(1+\epsilon) \sim 0 \tag{11}$$

where $G = P_2/P_1$, $\epsilon = kM_2^3 a_2 \cos\ \theta \mu_2 f''/(P_1 f')$, μ_2 is the gas viscosity near the separation point,and where the approximation $\tan\ \theta \approx -f'$ has been used. Under typical conditions, e.g., those extant in experiments described below [$M_i \approx 5$, $\theta \approx 16^o$, $T_o = 310$K, $P_o = 1.24$ Mpa], $\epsilon = O(10^{-3})$, i.e., $\epsilon << 1$ [where $f''|_{max} \approx (d\theta/dx)|_{max} = O(1)$]. Thus, solving (11) for P_p/P_1 and neglecting terms smaller than $O(\epsilon)$, we finally obtain

$$\frac{P_p}{P_1} \sim G - \epsilon\frac{2G}{G-1} \tag{12}$$

Importantly, this equation shows that $P_1/P_p \approx P_i/P_p \sim P_1/P_2$, *demonstrating that the separation pressure ratio essentially corresponds to the oblique shock pressure ratio.*

2.4 Shock and flow deflection angles

In order to close the approximate model embodied in (12), it is necessary to specify the shock angle, β, and the flow deflection angle, θ. Referring to earlier work, Summerfield et al. (Summerfield et al., 1954) used measured separation pressure ratios and Mach numbers in the oblique shock relations to infer θ; based on their data, they inferred a nominally fixed value, $\theta \approx 16^o$. By contrast, Ostlund (Ostlund, 2002), again using the same approach,argued that θ varies with M_i, albeit weakly; he fit his estimate with a linear relationship, $\theta = 1.678M_i + 9.347$, valid for $2.5 \leq M_i \leq 4.5$. For this range of M_i, however, the correlation indicates that θ only varies from 13.5^o and 16.9^o. Based on these indirect estimates, we assume that θ is constant; for simplicity, we will arbitrarily adopt the average value of θ indicated by Ostlund's correlation, $\theta \approx 15.2^o$, nearly equal to Summerfield's (Summerfield et al., 1954)

estimate. Second, we follow Summerfield (Summerfield et al., 1954) and assume that the oblique shock relation

$$\tan\theta = \frac{2\cot\beta(M_1^2\sin^2\beta - 1)}{(k+1)M_1^2 - 2(M_1^2\sin^2\beta - 1)} \tag{13}$$

applies to the inviscid flow outside the separating boundary layer.

2.5 Free interaction model

Chapman's (Chapman et al., 1958) original analysis posited that thickening of the boundary layer displacement thickness displaced the inviscid flow above the boundary layer according to

$$P(x) - P_i = \frac{\rho_i u_i^2}{\sqrt{M_i^2 - 1}} d\theta \tag{14}$$

where $d\delta^*/dx = d\theta$, and where the subscripts refer to conditions at x_i. He then estimated terms in the balance between the axial pressure gradient and cross-stream shear stress gradient as

$$\frac{P - P_i}{l_s} \sim \frac{\tau_{wi}}{\delta^*} \tag{15}$$

(where τ_{wi} is the wall shear stress near x_i), then estimated $d\delta^*/dx$ as δ^*/l_s (where $\delta^* \sim \delta_s$), and finally combined and linearized (for small $P - P_i$) to obtain

$$\frac{P - P_i}{q_i} \sim \frac{\sqrt{C_{fi}}}{(M_i^2 - 1)^{1/4}} \tag{16}$$

where $q_i = \rho_i u_i^2/2$ and $C_{fi} = \tau_{wi}/q_i$.
Dividing the left side of (16) by the right suggests that

$$\Big(\frac{P - P_i}{q_i}\Big)\Big(\frac{(M_i^2 - 1)^{1/4}}{\sqrt{C_{fi}}}\Big) \sim f(x - x_i) \tag{17}$$

i.e., that the term on the left depends only on position within the shock interaction zone. Erdos and Pallone (Erdos & Pallone, 1962) exploited this idea to develop a wall pressure correlation, $F(s)$, which describes the self-similar pressure variation over the shock interaction zone, where

$$F(s) = \Big(\frac{P - P_i}{q_i}\Big)\Big(\frac{(M_i^2 - 1)^{1/4}}{\sqrt{2C_{fi}}}\Big) \tag{18}$$

and where $s = (x - x_i)/(x_s - x_i)$. Carriere et al. (Carriere et al., 1968) extended this work by developing a generalized version of (18), suitable for the non- uniform flows in nozzles. In this case, the self-similar pressure variation over the separation zone is described by

$$F(s; p') = \sqrt{\Big(\frac{P - P_i}{q_i}\Big)\Big(\frac{\bar{\nu}(s) - \nu(s)}{\sqrt{C_{fi}}}\Big)} \tag{19}$$

where $p' = (\delta_i^*/q_i)(dP/dx)$ is the normalized inviscid flow pressure gradient immediately upstream of x_i, $\nu(s)$ is the Prandtl-Meyer function, and $\bar{\nu}(s)$ is the value of the function in the

absence of separation. For a range of pressure gradients observed in a number of different nozzles, the two correlations, $F(s)$ and $F(s;p')$, are nearly identical (Ostlund, 2002).
Given $F(s;p')$ (or $F(s)$), the predicted separation pressure ratio, P_i/P_p, can be determined from either (18) or (19); in the latter case, we follow Chapman (Chapman et al., 1958) and linearize (19) to obtain

$$\frac{P_i}{P_p} = \left[F(s_p;p')kM_i^2\left(\frac{\sqrt{C_{fi}}}{\sqrt{2}(M_i^2-1)^{1/4}}\right)+1\right]^{-1} \tag{20}$$

where $\bar{\nu}(s)$ is approximated as ν_i and where $F(s_p;p')$ [= 6.0; see (Ostlund, 2002)] is the value of $F(s;p')$ at the effective separation point, $s_p[=(x_p-x_i)/(x_s-x_i)]$. It is important to note that (Ostlund, 2002) has developed an alternative separation criterion which requires *a priori* specification of both the plateau pressure, P_p, and the friction coefficient, C_{fi} at x_i. The criterion in (20) by contrast only requires information on C_{fi}. Fortuitously, and as originally shown by Chapman (Chapman et al., 1958), for shock-induced separation of *turbulent* boundary layers, the dependence of P_i/P_p on C_{fi} (or equivalently, on $Re_{\delta*}$, the displacement thickness Reynolds number at x_i) is weak, at least over the range of Mach numbers investigated $(1.3 \leq M_i \leq 4.0)$, consistent with both the scale analysis above and previously developed correlations; see (Keanini & Brown, 2007) for further details.

2.6 Experimental measurements

A series of experiments were carried out in the Nozzle Test Facility at Marshall Space Flight Center (Keanini & Brown, 2007). The experiments were designed to investigate the role of boundary layer separation on nozzle side- loading and to examine fluid-solid interactions underlying oscillatory modes observed in side-loaded nozzles.
A sub-scale, ideal-contour nozzle, having an area ratio of approximately 30:1 (exit to throat area) was operated under a range of cold-flow, overexpanded conditions. The nozzle was outfitted with a series of pressure taps, where tap spacing in the axial direction was 0.0254 m. Two sets of azimuthally spaced taps were also used, placed at two axial locations, at 45^o intervals around the nozzle circumference. The axially-spaced taps allowed measurement of the instantaneous and time-average axial pressure distribution within the nozzle while the azimuthally distributed taps allowed examination of the instantaneous and time-average separation line (under conditions where the shock interaction zone coincides with either set of azimuthally distributed taps). The throat diameter was 0.0254 m and the design Mach number was 5.25. Pressures at all taps were sampled at 10 kHz, sufficiently high to allow study of the low-frequency, large-amplitude component of shock motion (Dolling & Brusniak, 1989; Keanini & Brown, 2007), but not sufficient to resolve small-scale, high frequency jitter.

2.7 Results

The scaling relationship in (12) was fit to available data on separation in overexpanded nozzles. Data on free shock separation was obtained from a number of sources (Keanini & Brown, 2007), and represents flow in a variety of nozzle geometries, in both full-scale and sub-scale models, under both cold flow and hot fire conditions. Although the working fluid in most experiments was air, Bloomer's (Bloomer et al., 1961) hot fire measurements, which used a mixture of JP-4 rocket fuel and liquid oxygen $(k = 1.2)$, are included in estimating best fit parameters. This approach is allowable due to the weak dependence between separation pressure ratio and k; see review in (Keanini & Brown, 2007). Since solutions for P_1/P_2 at a

turning angle of $\theta = 15.2^o$ do not exist for $M_i <\approx 1.7$, only data obtained at $M_i \geq 1.75$ are used in the fitting procedure. For comparative purposes, however, the limited data available at $M_i \leq 1.75$ are presented in the graphs below.

A comparison of separation pressure ratios predicted by the first scaling model (Keanini & Brown, 2007), model I in figures 4 and 5, with available data, shown in figure 4, indicates that the model provides reasonable predictions over the range $1.75 \leq M_i \leq 4.0$. The least square fitting constant is found to be 1.52 . A similar comparison using model II, Eq. (12), shown in figure 5, likewise indicates reasonable agreement over $1.75 \leq M_i \leq 4.5$, with significantly improved agreement for $M_i > 4.0$; the fitting constant in this case is 1.14. Comparing with Ostlund (Ostlund, 2002) and Frey's (Frey & Hagemann, 1998) correlations, which fit observed shock pressure ratios to the oblique shock pressure ratio (based on inferred shock and deflection angles), we note that their quoted ranges of validity were in both cases $2.5 \leq M_i \leq 4.5$. At higher Mach numbers $(M_i \geq 4)$, the data suggests that P_i/P_p becomes

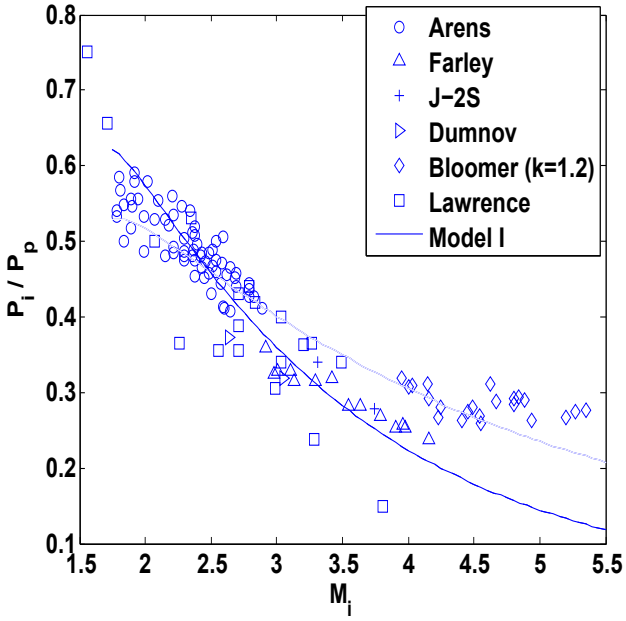

Fig. 4. Comparison of Model I in (Keanini & Brown, 2007) with separation measurements in rocket engine nozzles. The fitting constant equals 1.52.

largely independent of M_i. Although constancy of P_i/P_p is not inconsistent with separation remaining dominated by the oblique shock, since the asymptotic expression for P_i/P_p at large M_i is, from (12),

$$\frac{P_i}{P_p} \sim \frac{k+1}{2k\sin^2\beta M_i^2}$$

then due to an 82 % variation in M_i^2 over $4.0 \leq M_i \leq 5.4$, the time-average deflection angle, θ, likely becomes moderately dependent on M_i.

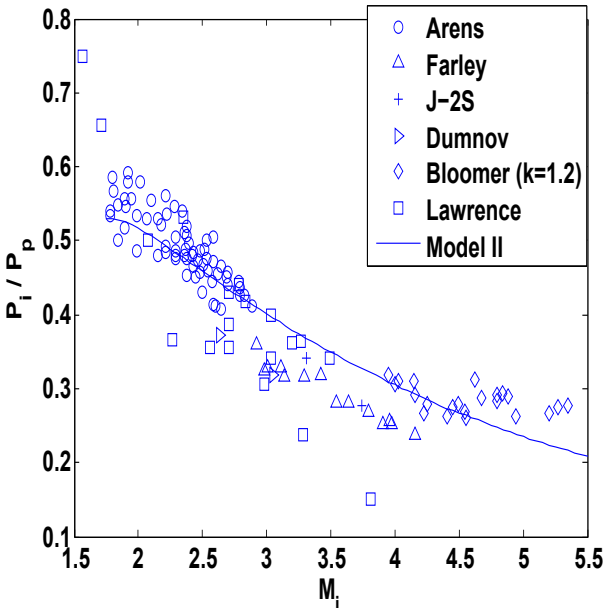

Fig. 5. Comparison of Model II (Keanini & Brown, 2007) with separation measurements in rocket engine nozzles. The fitting constant equals 1.14.

2.8 Separation pressure ratios via the free interaction model

In order to use the free interaction separation criterion in (20), C_{fi} must be specified. As noted, and based on Chapman's (Chapman et al., 1958) observation that P_i/P_p is weakly dependent on C_{fi}, we assume that C_{fi} is constant. The assumed magnitude, $C_{fi} = 0.00245$, represents the characteristic value obtained from fitting the free interaction model to observed time-average shock interaction zone pressure variations, as described in (Keanini & Brown, 2007). In addition, this value is used in fitting the generalized quasi-one-dimensional flow model, necessary for computing the flow upstream of the separation zone, to our experimental shock-free flow measurements; see (Keanini & Brown, 2007) for details.

As shown in figure 6, over $1.75 \leq M_i \leq 5.5$, predicted separation pressure ratios obtained via the free interaction model are quite similar to those obtained via the scaling analysis above. Given the reasonable agreement between model predictions and previous observations, this result simplifies Ostlund's (Ostlund, 2002) separation criterion by eliminating the need for *a priori* specification of P_p. Importantly, this result provides further evidence of the applicability of the free interaction model to separation in nozzles, and moreover, further indicates the physical consistency of the scale analyses presented in (Keanini & Brown, 2007).

3. Physically consistent models of random nozzle side loads

The models described in the previous section allow determination of the mean separation line position, $x_s(t) = x_s(H(t))$, within the nozzle, as a function of the instantaneous nozzle pressure ratio $NPR = NPR(H(t)) = P_o(t)/P_a(H(t))$ (Keanini & Brown, 2007; Keanini et al., 2011; Srivastava et al., 2010), where $P_o(t)$ is the time-dependent combustion chamber pressure

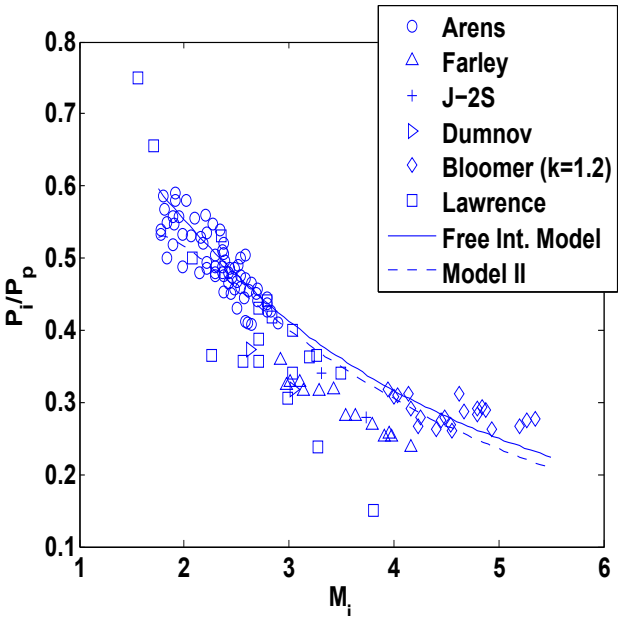

Fig. 6. Comparison of free interaction model and model II (Keanini & Brown, 2007) with separation measurements in rocket engine nozzles.

and $P_a(H(t))$ is the altitude- dependent ambient pressure. Given $x_s(t)$, physically consistent models that describe the stochastic evolution of the separation line *shape* relative to $x_s(t)$, can be developed. This section first highlights the essential elements of the stochastic side load models developed in (Keanini et al., 2011; Srivastava et al., 2010) and then briefly outlines a new, physically consistent model of stochastic separation line evolution (Keanini et al., 2011). As detailed in (Keanini et al., 2011; Srivastava et al., 2010), and in response to the decaying altitude-dependent ambient pressure, the mean position of boundary layer separation line, $x_s(t)$, travels down the nozzle axis toward the nozzle exit, with motion taking place on a relatively slow time scale, $\tau_a = \Delta x_a / V_R$, where Δx_a is the characteristic incremental altitude over which ambient pressure varies and V_R is the characteristic rocket speed. Superposed on this slow motion is a fast, random, azimuthally homogeneous stochastic motion. Following (Keanini et al., 2011; Srivastava et al., 2010), the joint probability density, p_s, associated with the instantaneous random separation line shape is given by

$$p_s(s_1, s_2, \ldots, s_N) = \prod_I p_I = \frac{1}{(2\pi\sigma_s)^{N/2}} \exp\left[- \frac{s_1^2 + s_2^2 + s_3^2 + \ldots + s_N^2}{2\sigma_s^2} \right] \tag{21}$$

where, as shown in figure 7, s_I is the random axial displacement of the separation line at azimuthal angle ϕ_I, and σ_s^2 is the (assumed) constant variance of local separation line displacements.

Constituent displacements in the set of N displacements are assumed independent, and based on experimental observations (Dolling & Brusniak, 1989), gaussian. Thus, each p_I is given by

$$p_I(s_I) = \frac{1}{\sqrt{2\pi\sigma_s^2}} \exp\Big[-\frac{s_I^2}{2\sigma_s^2}\Big] \tag{22}$$

In moving to a continuous description of the separation line, (Srivastava et al., 2010) assumes that

$$< s(\phi,t)s(\phi',t) >= \sigma_s^2\delta(\phi-\phi') \tag{23}$$

Considering next the side load, we express the instantaneous force vector produced by

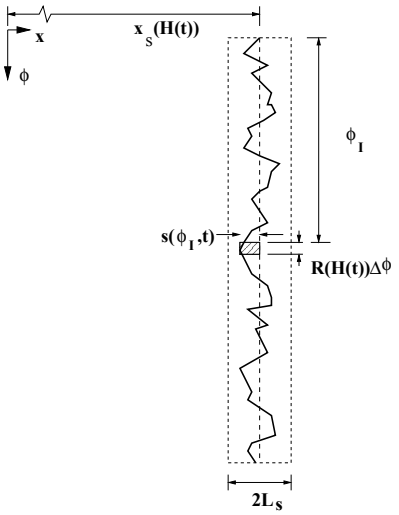

Fig. 7. Model I (Srivastava et al., 2010) separation line model. The mean separation line position, $x_s(H(t))$, moves down the nozzle axis, on the slow time scale associated with vertical rocket motion. By contrast, axial separation line motion about $x_s(H(t))$, at any angular position, ϕ_I, is random, and takes place on a much shorter time scale. Rapid axial motion, in addition, is confined to the nominal shock-boundary layer interaction zone, again denoted by L_s. Pressures upstream and downstream of the instantaneous separation line, $P_i = P_i(H(t))$ and $P_2 = P_2(H(t))$, respectively, are assumed to be spatially uniform within L_s. Adapted from (Srivastava et al., 2010).

asymmetric boundary layer separation, $\mathbf{F_s}(t)$, as a sum of radial and axial components

$$\mathbf{F_s}(t) = \mathbf{F_r}(t) + \mathbf{F_x}(t) \tag{24}$$

In (Srivastava et al., 2010), the following *ad hoc* side load model was assumed:

A) F_{sy} and F_{sz} are independent, gaussian random variables,

B) $< F_{sy} >= 0$ and $< F_{sz} >= 0$,

C) $\Big\langle \big(F_{sy} - < F_{sy} > \big)^2 \Big\rangle = \Big\langle \big(F_{sz} - < F_{sz} > \big)^2 \Big\rangle = \sigma^2$,

where, assuming ergodicity, $< \cdot >$ denotes either an ensemble or time average, and where the separation line model above is used to calculate the force variance σ^2. The side load components F_{sy} and F_{sz} are expressed with respect to rocket-fixed coordinates; see (Keanini et al., 2011; Srivastava et al., 2010).

In order to demonstrate the physical consistency of the model introduced in (Srivastava et al., 2010), (Keanini et al., 2011) first shows that the *assumed* properties, A) -C), can be *derived* from the simple *separation line model* developed in (Srivastava et al., 2010). Second, and as shown in the next subsection, the side load model in A) - C) then leads to *experimentally observed* side load amplitude and direction densities (Keanini et al., 2011).

3.1 Derivation of density functions for side load amplitude and direction

Two important experimental and numerical observations concerning the side load, $\mathbf{F_s}$ (within rigid, axisymmetric nozzles) are first noted:

a) the probability density of the random amplitude, $A = |\mathbf{F_s}|$, is a Rayleigh distribution (Deck & Nguyen, 2004; Deck et al., 2002), and

b) the random instantaneous direction, ϕ_s, of $\mathbf{F_s}$ is uniformly distributed over the periphery of the nozzle, or $p_{\phi_s}(\phi_s) = 1/2\pi$, where p_{ϕ_s} is the pdf of the side load direction (Deck & Nguyen, 2004; Deck et al., 2002).

Both observations can be *derived*, starting from the simple statistical model of random side loads, A) - C), immediately above. Thus, given A and ϕ_s, the instantaneous side load components in body-fixed y and z directions are given by

$$F_{sy} = A\cos\phi_s \qquad\qquad F_{sz} = A\sin\phi_s$$

Following (Srivastava et al., 2010), write F_{sy} and F_{sz} as $F_{sy} = \bar{Y} = A\cos\phi_s$ and $F_{sz} = \bar{Z} = A\sin\phi_s$; thus, the joint probability density associated with F_{sy} and F_{sz} can be expressed as

$$p_{\bar{Y}\bar{Z}}(\bar{Y},\bar{Z}) = p_{\bar{Y}}(\bar{Y})p_{\bar{Z}}(\bar{Z}) = \frac{1}{2\pi\sigma^2}\exp\left(-\frac{\bar{Y}^2+\bar{Z}^2}{2\sigma^2}\right) \tag{25}$$

Following (Srivastava et al., 2010), we restate $p_{\bar{Y}\bar{Z}}$ in terms of A and ϕ_s as,

$$p_{A\phi_s} = |J|p_{\bar{Y}\bar{Z}}(\bar{Y},\bar{Z}) \tag{26}$$

where $p_{A\phi_s}(A,\phi_s)$ is the joint pdf for the random amplitude and direction of $\mathbf{F_r}$, and where the jacobian determinant is given by

$$|J| = \left|\begin{array}{cc} \frac{\partial\bar{Y}}{\partial A} & \frac{\partial\bar{Y}}{\partial\phi_s} \\ \frac{\partial\bar{Z}}{\partial A} & \frac{\partial\bar{Z}}{\partial\phi_s} \end{array}\right| = A \tag{27}$$

Thus,

$$p_{A\phi_s}(A,\phi_s) = \frac{A}{2\pi\sigma^2}\exp\left(-\frac{A^2}{2\sigma^2}\right) = \left(\frac{1}{2\pi}\right)\left[\frac{A}{\sigma^2}\exp\left(-\frac{A^2}{2\sigma^2}\right)\right] = p_{\phi_s}(\phi_s)p_A(A) \tag{28}$$

where,

$$p_{\phi_s}(\phi_s) = \frac{1}{2\pi} \qquad\qquad 0 < \phi_s \leq 2\pi \tag{29}$$

is the uniform probability density underlying the random direction ϕ_s, and

$$p_A(A) = \frac{A}{\sigma^2} \exp\left(-\frac{A^2}{2\sigma^2}\right) \tag{30}$$

is the Rayleigh distribution for the amplitude A.

3.2 Ornstein-Uhlenbeck model of separation line dynamics

Theoretical determination of rocket response to side loads requires that the time correlation function for either side load component, $\langle F_{s\alpha}(t')F_{s\alpha}(t)\rangle$, be first determined. As detailed in (Keanini et al., 2011), $\langle F_{s\alpha}(t')F_{s\alpha}(t)\rangle$ is developed in two steps. First, and as detailed in this subsection, we propose(and physically justify) that local separation line dynamics can be modeled as an Ornstein-Uhlenbeck process. Once this assumption is made, then the second step rests on a rigorous argument showing that on the relatively long rocket dynamics time scale, the boundary layer separation line shape, and importantly, associated side load components, are all delta correlated in time. See (Keanini et al., 2011)for details.

The following simple, explicit stochastic model of separation line dynamics is proposed:

$$ds_i(t) = -ks_i(t) + \sqrt{D_s}dW(t) \tag{31}$$

where $s_i(t) = s(\phi_i, t)$ is the instantaneous separation line position at ϕ_i, k and D_s are damping and effective diffusion coefficients, and $dW(t)$ is a differential Weiner process. This equation, describing an Ornstein-Uhlenbeck process, allows straightforward, physically consistent calculation of statistical properties associated with separation line motion and, more importantly, serves as the first link in a chain that connects short-time-scale random separation line motion to short-time-scale random side loads, and in turn, to long-time-scale stochastic rotational rocket dynamics (Keanini et al., 2011).

The form of this equation is chosen based on the following experimental features, observed in shock-separated flows near compression corners and blunt fins:

a) Under statistically stationary conditions, the feet of separation-inducing shocks oscillate randomly, up- and downstream, over limited distances, about a fixed mean position; see, e.g., (Dolling & Brusniak, 1989).

b) As observed in (Dolling & Brusniak, 1989)the distribution of shock foot positions within the shock-boundary layer interaction zone is approximately gaussian.

c) The time correlation of shock foot positions, as indicated by wall pressure measurements within the shock-boundary layer interaction zone, decays rapidly for time intervals, $\triangle t$, larger than a short correlation time, τ_s, a feature that can be inferred, for example, from (Plotkin, 1975).

Physically, the damping term captures the fact that the shock sits within a pressure-potential energy well. Thus, downstream shock excursions incrementally decrease and increase, respectively, upstream and downstream shock face pressures; the resulting pressure imbalance forces the shock back upstream. A similar mechanism operates during upstream excursions. Introduction of a Weiner process models the combined random forcing produced by advection of turbulent boundary layer structures through the upstream side of the shock foot and pressure oscillations emanating from the downstream separated boundary layer and recirculation zone.

We note that the proposed model is qualitatively consistent with Plotkin's model of boundary layer-driven shock motion near compression corners and blunt fins (Plotkin, 1975). Plotkin's

model, which captures low frequency spectra of wall pressure fluctuations within these flows, corresponds to a generalized Ornstein-Uhlenbeck process in which a deterministic linear damping term is superposed with a non-Markovian random forcing term. We use an ordinary OU process model, incorporating a Weiner process, since again, it is consistent with the above observations and more particularly, since it allows much simpler calculation of statistical properties (Keanini et al., 2011).

4. Rocket response to random side loads

This section highlights recent results on numerical simulation of the stochastic ascent of a sounding-rocket-scale rocket, subjected to altitude dependent random nozzle side loads (Srivastava et al., 2010). The numerical simulations solve the full, coupled, nonlinear equations of rotational and translational rocket motion. The simulations include the effects of altitude-dependent aerodynamic drag forces, random nozzle side loads, associated random torques, mass flux damping torques (Keanini et al., 2011), and time-varying changes in rocket mass and longitudinal moment of inertia. In order to clearly isolate the effects of nozzle side loads on rocket translational and rotational dynamics, random wind loads are suppressed. A simple scaling argument (Keanini et al., 2011) indicates that random winds: i) under most conditions, do not excite rotational motion, and ii) simply function as an *additive* source of variance in the rocket's *translational* motion. In other words, wind appears to have minimal influence on the stochastic, altitude-dependent evolution of *rotational* dynamics. Rather, (launch-site-specific) mean and random winds simply produce whole-rocket, random, *lateral translational* motion, superposed on a deterministic translational drift.

Given side load direction and amplitude densities in Eqs. (29) and (30), respectively, altitude- dependent side loads are simulated using a Monte Carlo approach; the nonlinear, coupled equations of translational and rotational motion are then solved using fourth order Runge-Kutta integration (Srivastava et al., 2010). In estimating altitude-dependent means and variances in translational and rotational velocities and displacements, an ensemble of 100 simulated flights are used; it is found that estimated statistics do not vary significantly when using ensembles of 40 and 100 flights (Srivastava et al., 2010). The parameters employed in the simulations are characteristic of medium sized sounding rockets (Srivastava et al., 2010).

Characteristic results are presented in figures 8 through 13. The stochastic evolution of both lateral side load components, F_{sy} and F_{sz}, observed during a single simulated realization, is shown in figure 8. Initially, i.e., at launch, the pressure jump across the separation-inducing shock is relatively high (Srivastava et al., 2010), and is manifested by somewhat higher initial side load amplitudes. However, as the rocket gains altitude, ambient pressure decays, and the cross-shock pressure jump decreases - characteristic side load magnitudes become smaller. At the instant when the slowly traveling in-nozzle shock reaches the nozzle exit, the nozzle flow becomes shock free, boundary layer separation ceases, and side loading stops. For these simulations, this instant corresponds to a flight time of 10.85 seconds (Srivastava et al., 2010), or an altitude of approximately 3.75 km. Note that side load amplitudes are significant, on the order of 10 to 16 % of the rocket's initial weight.

Figure 9 shows a single realization of the rocket's trajectory, under the action of random side loads, and is compared against the trajectory taken when side loads are suppressed. [Here, and throughout, X_o and (Y_o, Z_o) denote, respectively, the vertical, and (mutually orthogonal) lateral displacements of the rocket center of mass, relative to the launch location.] It is clear, that absent active control, a rocket can exhibit significant lateral displacements relative to the predicted zero-side-load path. Scaling shows that the characteristic magnitudes of random

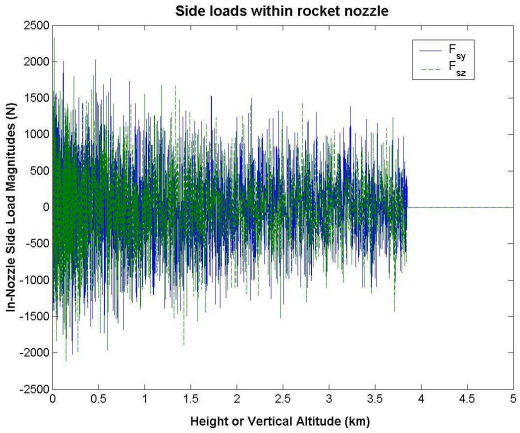

Fig. 8. In-nozzle stochastic side loads versus rocket altitude. Adapted from (Srivastava et al., 2010).

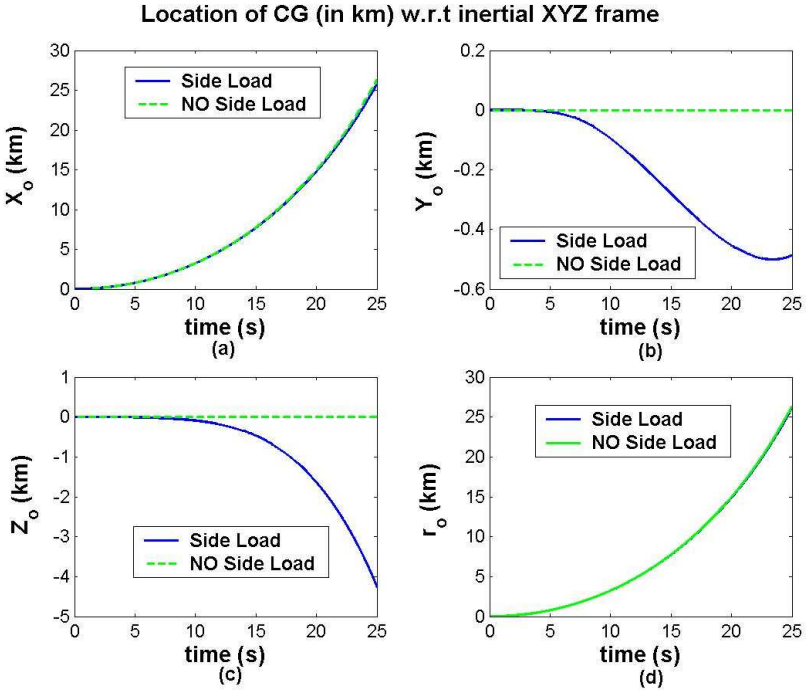

Fig. 9. Single realizations of rocket center of mass trajectory under random side loads and with side loads suppressed. X_o, and (Y_o, Z_o) denote, respectively, the vertical, and (mutually orthogonal) lateral displacements of the rocket center of mass, relative to the launch location. Adapted from (Srivastava et al., 2010).

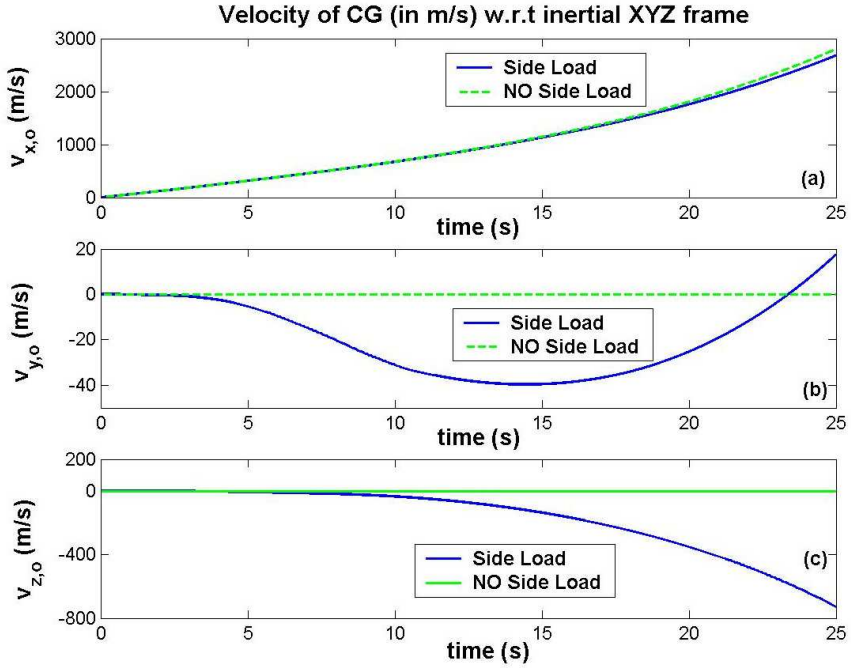

Fig. 10. Single realizations of rocket center of mass velocity under random side loads and with side loads suppressed. $v_{x,o}$ and $(v_{y,o}, v_{z,o})$, denote, respectively, the vertical, and (mutually orthogonal) lateral velocities of the rocket center of mass, relative to the launch location. Adapted from (Srivastava et al., 2010).

lateral displacements, which can be on the order of 1-4 kilometers over the simulated flight time of 25 seconds, are fully consistent with displacements estimated using characteristic side load magnitudes (Keanini et al., 2011; Srivastava et al., 2010). The several order of magnitude difference between (vertical) thrust forces and the small vertical component of $\mathbf{F_s}$ explains the result shown in figure 8a.

Random side loads produce significant excitation of pitch and yaw dynamics (Keanini et al., 2011; Srivastava et al., 2010). Thus, for example, once a rocket begins a random pitching and yawing motion, that motion continues, even after side loading stops (at $t = 10.85$ s). Random pitch and yaw, in turn, produce random lateral velocities. As indicated in figures 10 and 11, and as discussed in detail in (Keanini et al., 2011), a certain amount of time - an induction period - must pass before side-load-induced pitch and yaws grow large enough for significant lateral thrust components to appear. Once the induction period has passed, however, large lateral thrusts begin to act and the rocket begins to experience large lateral velocities and displacements. Figures 10 and 11 capture these essential dynamical features. The work in (Keanini et al., 2011) provides a detailed, physically-based analysis of the complex dynamics a rocket experiences during side loading.

As shown in (Keanini et al., 2011), and as indicated in figure 12, stochastic pitch and yaw rotational dynamics are characterized by two qualitatively distinct regimes. During the side load period, $t \leq 10.85$ s, the action of random side loads on pitch and yaw angular velocities

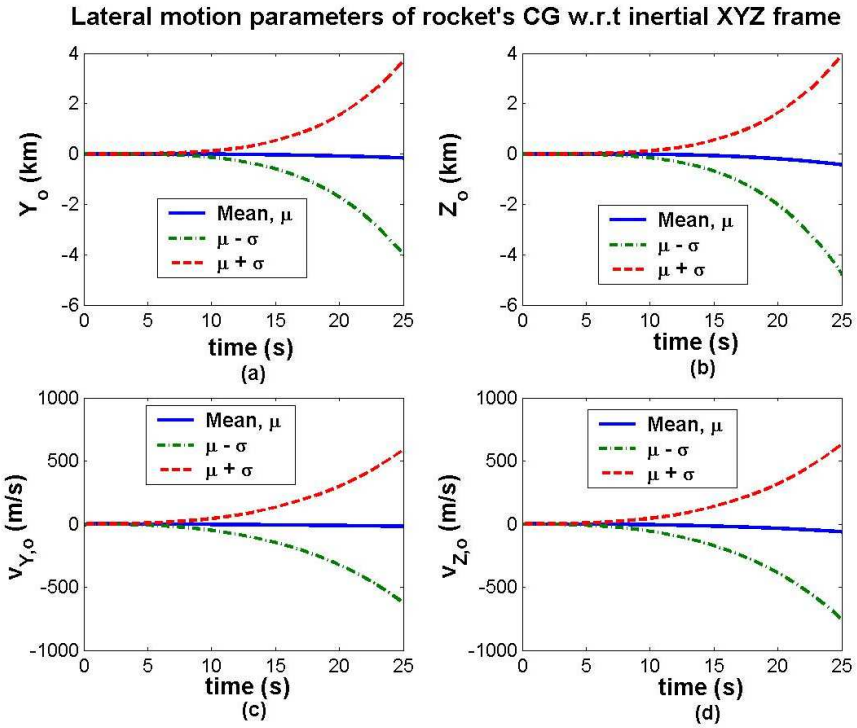

Fig. 11. Time-(altitude-)dependent means and variances of the rocket's lateral center of mass position (Y_o, Z_o) and lateral center of mass velocity (v_{yo}, v_{zo}). Adapted from (Srivastava et al., 2010).

can be modeled as an Ornstein-Uhlenbeck process, wherein side loads function, at least on the long rocket dynamics time scale, as Weiner processes. Simultaneous to stochastic pitch/yaw amplification, deterministic pitch/yaw damping, produced by incremental changes in the nozzle mass flux vector, i.e., mass flux damping (Keanini et al., 2011), counteract amplification. Thus, during the side load period, pitch/yaw velocities grow, but at an ever-decreasing rate. In the second regime, which begins when the separation-inducing shock exits the nozzle and side loads cease, mass-flux damping continues, driving pitch and yaw velocities toward zero (Keanini et al., 2011). These qualitative features are likewise apparent in plots of time-(altitude-)dependent pitch/yaw means and variances; see figure 13. As detailed in (Keanini et al., 2011), all of these features can be rigorously explained using, e.g., a course grained description of short-time-scale side load statistics, along with an asymptotic model of rocket translational and rotational motion.

5. Stochastic rocket ascent as a diffusion process

Starting with the nonlinear equations of rotational motion, (Keanini et al., 2011) use a rigorous argument to show that the equations governing evolution of pitch and yaw rates assume the

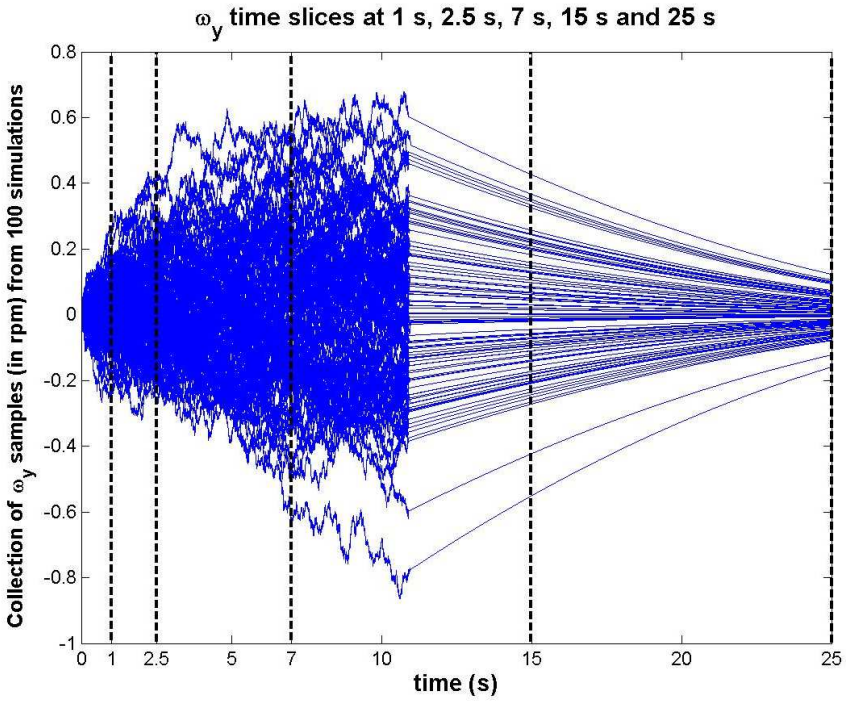

Fig. 12. Ensemble of 100 realizations of yaw angular velocity evolution. Side loads cease at $t = 10.85$ s. Adapted from (Srivastava et al., 2010).

form of an Ornstein-Uhlenbeck process:

$$d\omega_{\pm} = -A(t)\omega_{\pm} \pm \sqrt{D(t)}dW_{\pm} \tag{32}$$

where $\omega_{+} = \omega_y$ and $\omega_{-} = \omega_z$ correspond, respectively, to yaw and pitch rate, $A(t)$ and $D(t)$ are, respectively, the time-(altitude-)dependent effective damping and diffusion coefficients, and $W_{\pm}(t)$ are Weiner processes.

Fundamentally, and as detailed in (Keanini et al., 2011), equation (32) provides the key to analyzing both the rotational and translational rocket response to side loading. Physically, $A(t)$ is roughly proportional to both the squared moment arm from the rocket center of mass to the nozzle exit, L_{ce}^2, as well as the mass flux magnitude, and is inversely proportional to the lateral moment of inertia. Likewise, $D(t)$ is proportional L_{ce}^2, as well as the squared (altitude-dependent) pressure difference between the interior and exterior of the nozzle, and the squared altitude-dependent position of the separation-inducing shock.

Practically, the detailed formulas for $A(t)$ and $D(t)$ in (Keanini et al., 2011) are related to both rocket-specific design parameters, as well as universal, non-specific parameters characterizing in-nozzle, shock-boundary layer separation. Thus, as discussed in (Keanini et al., 2011), the formulas allow straightforward identification of design criteria for, e.g., enhancing pitch/yaw damping and/or suppressing diffusive, i.e., stochastic growth of random pitch and yaw.

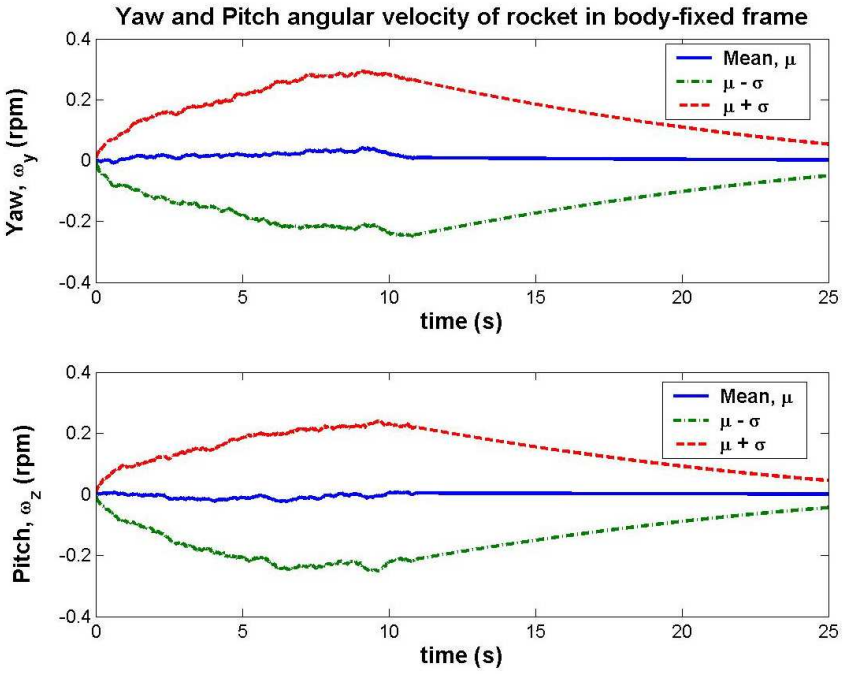

Fig. 13. Time-(altitude-)dependent means and variances of the rocket's pitch and yaw angular velocities. Adapted from (Srivastava et al., 2010).

6. References

Bloomer, H. E., Antl, R. J. & Renas, P. E. (1961). Experimental study of the effects of geometric variables on performance of conical rocket engine exhaust nozzles, NASA TN D-846.

Carriere, P., Sirieix, M. & Solignac, J. L. (1968). Properties de similitude des phenomenes de decollement laminaires ou turbulents en ecoulement supersonic nonuniforme, *12th Int. Congress of Applied Mech.*, Stanford Univ., Palo Alto, CA.

Chapman, D. R., Kuehn, H. K. & Larson, H. K. (1958). Investigation of separated flows in supersonic and subsonic streams with emphasis on the effect of transition, NACA Report 1356.

Deck, S. & Nguyen, A. T. (2004). Unsteady side loads in thrust-optimized contour nozzle at hysteresis regime, *AIAA J.*, Vol. 42, No. 9, pp. 1878-1888.

Deck, S., Garnier, E. & Guillen, P. (2002). Turbulence modeling applied to space launcher configurations, *J. Turbulence*, Vol. 3, No. 1, pp. 57-57(1).

Dolling, D. S. & Brusniak, L. (1989). Separation shock motion in fin, cylinder, and compression ramp-induced turbulent interactions, *AIAA J.*, Vol 27, No. 6, pp. 734-742.

Erdos, J. & Pallone, A. (1962). Shock-boundary layer interaction and flow separation, *Proc Heat Transfer and Fluid Mechanics Institute*, Stanford Univ. Press.

Flemming, E. L., Chandra, S., Schoeberl, M. R. & Barnett, J. J. (1988). Monthly Mean Global Climatology of Temperature, Wind, Geopotential Height, and Pressure for 0-120 km, NASA TM-100697.

Frey, M. & Hagemann, G. (1998). Status of flow separation prediction in rocket nozzles, AIAA Paper 98-3619.

Gruntman, M. (2004). *Blazing The Trail: The Early History Of Spacecraft and Rocketry,* AIAA, Reston, VA.

Justus, C. G. & Johnson, D. L. (1999). The NASA/MSFC Global Reference Atmospheric Model -1999 Version, NASA TM-1999-209630.

Justus, C. G., Campbell, C. W., Doubleday, M. J. & Johnson, D. L. (1990). New Atmospheric Turbulence Model for Shuttle Applications, NASA TM-4168.

Keanini, R. G. & Brown, A. (2007). Scale analysis and experimental observations of shock-induced turbulent boundary layer separation in nozzles, *European J. Mechanics B/Fluids,* Vol. 26, pp. 494-510.

Keanini, R. G., Srivastava, N. & Tkacik, P. T. (2011). Stochastic rocket dynamics under random nozzle side loads: Ornstein-Uhlenbeck boundary layer separation and its course grained connection to side loading and rocket response, in press *Annalen der Physik.*

Leahy, F. B. (2008). Discrete gust model for launch vehicle assessements, 12th *Conf. on Aviation, Range and Aerospace Metrology,* Atlanta, GA, Jan. 2006, American Meteorology Society..

McNaughtan, I. I. (1993). The resistance of transparencies to bird impact at high speeds, *Aircraft Engrg. Aerospace Tech.,* Vol. 36, No. 12, pp. 409-413.

Ostlund, J. (2002). Supersonic flow separation with application to rocket engine nozzles, Doctoral Thesis, Department of Mechanics, Royal Institute of Technology, Stockholm, Sweden.

Plotkin, K. J. (1975). Shock wave oscillation driven by turbulent boundary-layer fluctuations, *AIAA J.,* Vol. 13, No. 8, pp. 1036-1040.

Schmucker, R. H. (1984). Flow Processes in Overexpanded Chemical Rocket Nozzles - Part I, NASA Rep. 77396.

Sekita, R., Watanabe, A., Hirata, K. & Imoto, T. (2001). Lessons learned from H-2 failure and enhancement of H-2A project, *Acta Astronautica,* Vol. 48, No. 5-12, pp. 431-438.

Srivastava, N., Tkacik, P. T. & Keanini, R. G. (2010). Influence of nozzle random side loads on launch vehicle dynamics, *J. Applied Physics,* Vol. 108, pp. 044911-044926.

Summerfield, M., Foster, C. R. & Swan, W. C. (1954). Flow separation in overexpanded supersonic exhaaust nozzles, *Jet Propulsion,* Vol. 24, No. 9, pp. 319-321.

Sutton, G. P. & Biblarz, O. (2001). *Rocket Propulsion Elements, 7th ed,* Wiley, New York.

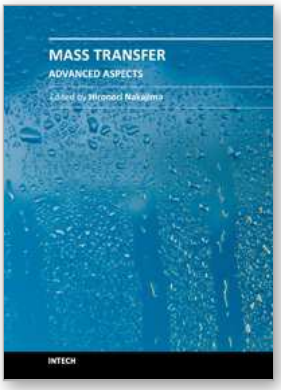

Mass Transfer - Advanced Aspects

Edited by Dr. Hironori Nakajima

ISBN 978-953-307-636-2
Hard cover, 824 pages
Publisher InTech
Published online 07, July, 2011
Published in print edition July, 2011

Our knowledge of mass transfer processes has been extended and applied to various fields of science and engineering including industrial and manufacturing processes in recent years. Since mass transfer is a primordial phenomenon, it plays a key role in the scientific researches and fields of mechanical, energy, environmental, materials, bio, and chemical engineering. In this book, energetic authors provide present advances in scientific findings and technologies, and develop new theoretical models concerning mass transfer. This book brings valuable references for researchers and engineers working in the variety of mass transfer sciences and related fields. Since the constitutive topics cover the advances in broad research areas, the topics will be mutually stimulus and informative to the researchers and engineers in different areas.

How to reference

In order to correctly reference this scholarly work, feel free to copy and paste the following:

R. G. Keanini, T. D. Nortey, Karen Thorsett-Hill, N. Srivastava, Sam Hellman, P. T. Tkacik and P. Douglas Knight (2011). Shock-Induced Turbulent Boundary Layer Separation in Over-Expanded Rocket Nozzles: Physics, Models, Random Side Loads, and the Diffusive Character of Stochastic Rocket Ascent, Mass Transfer - Advanced Aspects, Dr. Hironori Nakajima (Ed.), ISBN: 978-953-307-636-2, InTech, Available from: http://www.intechopen.com/books/mass-transfer-advanced-aspects/shock-induced-turbulent-boundary-layer-separation-in-over-expanded-rocket-nozzles-physics-models-ran

INTECH
open science | open minds

InTech Europe
University Campus STeP Ri
Slavka Krautzeka 83/A
51000 Rijeka, Croatia
Phone: +385 (51) 770 447
Fax: +385 (51) 686 166
www.intechopen.com

InTech China
Unit 405, Office Block, Hotel Equatorial Shanghai
No.65, Yan An Road (West), Shanghai, 200040, China
中国上海市延安西路65号上海国际贵都大饭店办公楼405单元
Phone: +86-21-62489820
Fax: +86-21-62489821